# Proton capture cross sections on neutron-magic $^{144}$Sm at astrophysically relevant energies

N. Kinoshita,[1,*] K. Hayashi,[2] S. Ueno,[2] Y. Yatsu,[2] A. Yokoyama,[3] and N. Takahashi[4]
[1]*Institute of Technology, Shimizu Corporation, 3-4-17 Etchujima, Koto-ku, 135-8530 Tokyo, Japan*
[2]*Graduate School of Natural Science and Technology, Kanazawa University, Kakuma-machi, Kanazawa, 920-1192 Ishikawa, Japan*
[3]*Institute of Science and Engineering, Kanazawa University, Kakuma-machi, Kanazawa, 920-1192 Ishikawa, Japan*
[4]*Graduate School of Science, Osaka University, 1-1 Machikaneyama, Toyonaka, 560-0043 Osaka, Japan*
(Received 26 March 2015; revised manuscript received 26 October 2015; published 2 February 2016)

**Background:** The $p$ nuclei, which are not produced by neutron capture processes, are present with a typical isotopic abundance of 0.01%–0.3%. Abundance decreases with an increase in atomic number. However, the neutron-magic isotopes of $^{92}$Mo and $^{144}$Sm exhibit unusually large abundances in comparison. A combination of proton and $\alpha$-particle capture reactions and neutron emission reactions are key to understanding this issue. Currently, complex network calculations do not have access to much experimental data, and hence require theoretically predicted reaction rates in order to estimate final abundances produced in nucleosynthesis.
**Purpose:** Few experimental cross sections of $(p,\gamma)$ reactions on heavy nuclides with mass numbers of 130–150 have been reported. The $^{144}$Sm$(p,\gamma)$ $^{145}$Eu reaction is the main destruction pathway for the nucleosynthesis of the $^{144}$Sm nuclide. In the present paper, experimental cross sections of the $^{144}$Sm$(p,\gamma)$ $^{145}$Eu reaction at a range including astrophysically relevant energies for the $p$ process were determined to compare with theoretical predictions using the Hauser-Feshback statistical model.
**Methods:** The $^{144}$Sm was deposited on a high-purity Al foil with the molecular plating method. Stacks consisting of Ta degrader foils, $^{144}$Sm targets, and Cu foils used as flux monitors were irradiated with 14.0-MeV proton beams. The $^{144}$Sm$(p,\gamma)$ $^{145}$Eu cross sections were determined from the $^{145}$Eu activities and the proton fluence estimated from the $^{65}$Zn activity in the Cu monitor foil. The proton energies bombarded on each $^{144}$Sm target were estimated using SRIM2013.
**Results:** We determined the $^{144}$Sm$(p,\gamma)$ $^{145}$Eu cross sections at proton energies between 2.8 and 7.6 MeV. These energies encompass nucleosynthesis temperatures between 3 and 5 GK. The cross sections at energies higher than 3.8 MeV agreed well with theoretically predicted cross sections using TALYS using the generalized superfluid (GS) model for level densities. However, calculations using NON-SMOKER overestimated the cross section. When the components of the energy uncertainties in the experimental cross sections were corrected, the cross sections at energies lower than 3.8 MeV showed comparable values with TALYS but higher than those predicted by both NON-SMOKER and TALYS.
**Conclusions:** TALYS using the GS model reproduced well the experimental cross sections without correction of the proton widths at energies between 2.8 and 7.6 MeV. Thus, the reaction rates of $^{144}$Sm$(p,\gamma)$ $^{145}$Eu in the stellar environment at 2.5–5 GK estimated with TALYS corresponded with those by the experimental cross section within 10%. However, the reaction rates depended on the extrapolation of the cross section at energies of 0–2.8 MeV at temperatures of 0.5–2.5 GK. The reaction rate estimated by TALYS employing the GS model showed an uncertainty within a factor of 2 at 1.5–3.5 GK for nucleosynthesis temperatures of the $p$ nuclei.

DOI: 10.1103/PhysRevC.93.025801

## I. INTRODUCTION

Most elements heavier than iron are synthesized via neutron capture processes known as the $s$ process and the $r$ process [1,2]. However, in the solar system, there are 35 neutron-deficient stable isotopes between Se and Hg with low isotopic abundance comparing to nuclei produced by the $s$ and $r$ processes. These nuclei, not created by the $s$ process or $r$ process, are termed $p$ nuclei. The $p$ process, by which $p$ nuclei are synthesized, proceeds via photodisintegration reactions [3–5], proton capture reactions [6,7], and neutrino processes [8] on the preexisting heavy $s$ and $r$ seed nuclei at temperatures between 1.5 and 3.5 GK. These high temperatures can be obtained in explosive environments, such as in the O/Ne layers of type-II supernovae and in the deflagration flame fronts of type-Ia supernovae [9,10].

The $p$ nuclei are present in the solar system with an isotopic abundance of approximately 1% for lighter nuclei with atomic numbers of 34–50 and 0.01%–0.3% for medium and heavier nuclei with atomic numbers larger than 50 [11]. Generally, the abundance of $p$ nuclei decreases with an increase in atomic number. On the other hand, the neutron-magic $p$ nuclei of $^{92}$Mo and $^{144}$Sm present isotopic abundances of 14.52% and 3.08%, respectively [12,13]. The neutrino process is a strong candidate for the nucleosynthesis of $^{92}$Nb, $^{136,138}$Ce, and $^{138}$La [14,15]. However, the neutrino process cannot well explain the greater abundance of $^{92}$Mo and $^{144}$Sm. Photodisintegration as well as the capture reaction of charged particles are considered to explain these abundances.

Reaction rates in a stellar environment are calculated from the product of the reaction cross section and the energy

*Corresponding author: norikazu.kinoshita@shimz.co.jp

 

spectrum of particles or photons [5,16]. The Maxwell-Boltzmann distribution and Planck's blackbody spectrum are used to describe the spectra of a particle and photon, respectively. The $^{144}$Sm can be produced via proton capture on Nd seed nuclei, and it can also be produced by neutron emission from heavier Sm isotopes which are also *r* and *s* process seed nuclei. The $^{144}$Sm$(p,\gamma)$ $^{145}$Eu reaction is the destruction pathway for the nucleosynthesis of the $^{144}$Sm nuclide. The final abundance of nuclei in the nucleosynthesis can be estimated with a mass balance between reaction rates of production and destruction [7]. The photodisintegration reaction rates increase drastically with an increase in temperature above ∼1 GK according to the Hauser-Feshback statistical model as calculated using TALYS [16]. When hydrogen is present with a density of 1000 g cm$^3$ in the nucleosynthesis environment, TALYS gives a comparable reaction rate at ∼2 GK in $^{143}$Pm$(p,\gamma)$ and $^{145}$Sm$(\gamma,n)$ reactions, and the $(\gamma,n)$ reaction is dominant at temperatures higher than 2 GK in the production of $^{144}$Sm. Thus, instead of photodisintegration, proton capture reactions are important in the production and destruction of $^{144}$Sm at temperatures lower than ∼2 GK. A combination of proton and charged particle capture reactions and neutron emission reactions would understand the abundance. Generally, neutron-deficient nuclei have a higher threshold of neutron emission. On the other hand, the threshold of the $(\gamma,n)$ reaction is lower with an increase in atomic number; photodisintegration easily occurs in heavier nuclei with larger atomic numbers. The capture reaction of a charged particle becomes more difficult with an increase in atomic number because of the increase in the Coulomb barrier in the fusion reaction. Theoretical calculations are sufficient to determine the reaction network synthesis of $^{144}$Sm, but the purpose of the present paper is to validate the theoretical calculations with experimental data.

Somorjai *et al.* [17] reported the $^{144}$Sm$(\alpha,\gamma)$ $^{148}$Gd destruction cross section at energies between 10 and 13 MeV, which comprises the region of ∼5 GK in nucleosynthesis. The cross sections down to 83 nb have been successfully determined. However, the Hauser-Feshbach prediction using NON-SMOKER [18] presented cross sections an order of magnitude greater than the measurements. On the other hand, the $^{144}$Sm$(\gamma,n)$ $^{143}$Sm cross sections around the threshold were determined using bremsstrahlung [19]. The $^{144}$Sm$(\gamma,n)$ $^{143}$Sm cross sections with the theoretical prediction using TALYS agreed well with the experimental values of the cross section. Recently, the proton capture reaction on the *p* nucleus $^{130}$Ba has been reported [20]. Cross sections down to 3.6 MeV were determined and compared with theoretical predictions obtained using TALYS. In the present paper, we measured the $^{144}$Sm$(p,\gamma)$ $^{145}$Eu cross-sectional values to experimentally obtain reaction rates of the destruction process in the proton capture reactions. The cross sections were compared with theoretical data obtained using NON-SMOKER and TALYS to understand which factors in a nuclear model cause differences between measurement and theoretical values. Moreover, we estimated proton capture reaction rates for the ground state of $^{144}$Sm by extrapolating the cross section to lower energies than that at which it was measured.

## II. EXPERIMENT

Two kinds of target stacks were individually bombarded by 14-MeV proton beams. One stack consisted of a Ta degrader foil, a $^{144}$Sm target, and a Cu monitor foil. The other stack consisted of a Ta degrader and six $^{144}$Sm targets. The $^{144}$Sm was deposited on a pure Al foil using the molecular plating method [21]. The bombarding proton energies on each target were calculated using SRIM2013 [22]. After irradiation, the residual $^{145}$Eu activity ($T_{1/2} = 5.93 \pm 0.04$ d) in the $^{144}$Sm target and $^{65}$Zn activity ($T_{1/2} = 243.93 \pm 0.09$ d) in the Cu monitor foil were determined with an high-purity (HP)Ge detector [23,24]. The $^{144}$Sm$(p,\gamma)$ $^{145}$Eu cross sections were determined from the beam current as obtained from the monitor reactions, thickness of the $^{144}$Sm target, activity of $^{145}$Eu, and irradiation time. Details of the experimental procedure and data analysis are described below.

### A. Target preparation

Targets of $^{144}$Sm were prepared in a similar manner as reported by Parker *et al.* [21]. Oxides of 94.4% enriched $^{144}$Sm were dissolved in $HNO_3$ and then diluted to approximately 1000 ppm with de-ionized water. Some 0.1 ml of the solution was evaporated; the residue was dissolved in 3 ml of isopropyl alcohol. The alcohol solution was transferred to a Teflon cell [25] with a 37.0 mm$^2$ deposition area. The installed Al high-purity foil and spiral platinum wire soaked in solution were connected to a cathode and anode, respectively; 500 V were applied between the electrodes for 10 min. After the alcohol solution was removed, the $^{144}$Sm target was dried in ambient temperature. This procedure was highly efficient with only 10% of the dissolved $^{144}$Sm remaining in solution after the target fabrication. The $^{144}$Sm was deposited on 50-$\mu$m- and 100-$\mu$m-thick Al foils with 99.999% purity. Also, $^{144}$Sm content in the original 1000-ppm solution and in the alcohol solution removed after the molecular plating process were measured with an inductively coupled plasma mass spectrometer. The thickness of the target was calculated from the amount of $^{144}$Sm used for molecular plating, the amount of $^{144}$Sm which was not deposited, and the deposition area. The $^{144}$Sm targets of approximately 200 $\mu$g cm$^2$ with uncertainties of 4%–7% were prepared.

### B. Target stack and activation

Three stacks were prepared for the measurements of the cross sections. One stack (hereafter termed the monitor stack) consisted of a 200-$\mu$m-thick Ta degrader foil, a $^{144}$Sm target, and a 10-$\mu$m-thick natural Cu foil with the same area as the $^{144}$Sm target, placed on an Al foil. The other stacks (hereafter termed target stacks 1 and 2) consisted of a 200-$\mu$m-thick Ta degrader foil and six $^{144}$Sm targets. In target stack 2, a 20-$\mu$m-thick Al degrader foil was installed between the first and the second $^{144}$Sm targets to obtain data at different energies. Schematics of the stacks are shown in Fig. 1.

Activation with the proton beams was carried out at the Research Center for Nuclear Physics (RCNP), Osaka University. Some 2-$\mu$A proton beams accelerated using an AVF cyclotron to 14.0 MeV with <0.1% energy uncertainty

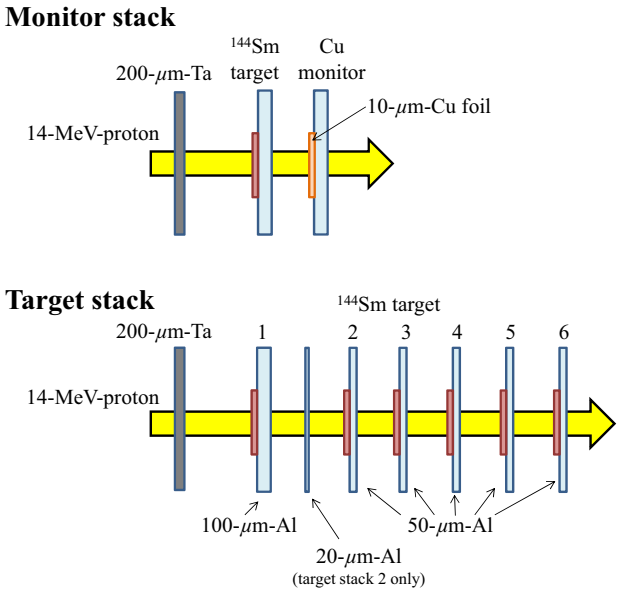


FIG. 1. Arrangement of the monitor and target stacks. The 20-$\mu$m-thick Al foil was not installed in target stack 1 but was placed between the first and the second $^{144}$Sm target in target stack 2.

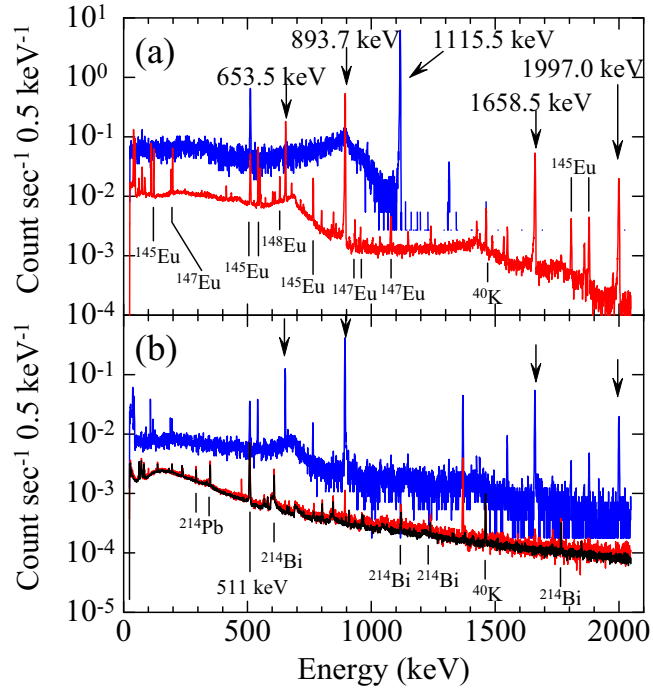


FIG. 2. (a) $\gamma$-ray spectra of the Cu monitor foil and $^{144}$Sm target in the monitor stack. (b) $\gamma$-ray spectra of the detector background (black line), $^{144}$Sm targets activated by 5.4 MeV (blue line), and 2.8 MeV (red line) in the target stack.

were introduced into a vacuum irradiation chamber [26]. The monitor stack and target stacks were individually irradiated in the chamber for 30 min and 3 h, respectively. The stacks were water cooled during the irradiation.

In the activation of the monitor stack, the beam energy decreased in the Ta degrader as well as in the Al foils in the $^{144}$Sm targets and in the Cu foil. In the target stacks, the beam energy decreased in the Ta degrader to the same energy as in the monitor stack and in the Al foils of the six $^{144}$Sm targets. We therefore obtained cross sections for 11 energies.

### C. Calculation of proton energy

The bombarding proton energies of each target were calculated with SRIM2013 [22]. The SRIM calculation showed good agreement with experimental data within 1% for both Al at 2–8 MeV [27,28] and Ta at 6–14 MeV [29]. In the monitor stack, the energy of the proton beam decreased from 14.00 $\pm$ 0.01 to 7.57 $\pm$ 0.15 MeV in the Ta degrader and to 6.36 $\pm$ 0.19 MeV in the 100-$\mu$m-thick Al backing foil. In addition, the energy was decreased by 0.30 MeV in the 100-$\mu$m-thick Cu foil. The $^{144}$Sm and Cu foils in the monitor stack were activated by protons with energies of 7.57 $\pm$ 015 and 6.06–6.36 MeV, respectively. On the other hand, target stack 1 produced energy data of 7.57 $\pm$ 0.15, 6.36 $\pm$ 0.19, 5.69 $\pm$ 0.19, 4.97 $\pm$ 0.22, 4.15 $\pm$ 0.26, and 3.19 $\pm$ 0.30 MeV. Target stack 2 with 20-$\mu$m-thick Al installed as a degrader provided energy values of 7.57 $\pm$ 0.15, 6.06 $\pm$ 0.19, 5.37 $\pm$ 0.21, 4.62 $\pm$ 0.23, 3.75 $\pm$ 0.28, and 2.81 $\pm$ 0.35 MeV. Concerning the uncertainties in the bombarding proton energies, the uncertainties were estimated with a Monte Carlo simulation code of PHITS [30] employing ATIMA [31,32] for the energy loss and straggling. According to the simulation, the energy spectra showed a Gaussian distribution by struggling in the energy loss. We considered $1\sigma$ of the spectra caused by the struggling, 0.1% uncertainty in the initial proton energy, and 0.01% uncertainty in weighing the Ta and Al foils. The energy loss was regarded to be less than 10 keV in the $^{144}$Sm deposited material on the Al foils. The energies and uncertainties are summarized in Table I together with the results of the cross sections.

### D. $\gamma$-ray spectrometry and data analysis

After cooling for 1–5 days, each target was measured with an HPGe detector with 100% relative efficiency. The detector was shielded by 15-cm-thick lead bricks to measure ultralow $^{145}$Eu activities. The $^{144}$Sm target and Cu foil in the monitor stack were measured at a position of 10 cm from the surface of the detector. Subsequently, all the $^{144}$Sm targets in both the monitor and the target stacks were measured at 1 cm from the surface of the detector for 5 min to 4 days for accumulating more than 1000 counts in the largest $\gamma$-ray peak of 893.7 keV. Spectra of the $^{144}$Sm and Cu targets are shown in Fig. 2 as examples. Clear peaks of $^{65}$Zn and $^{145}$Eu were identified from the Cu foil and $^{144}$Sm target in the monitor stack. The $^{145}$Eu activity was successfully determined in the samples irradiated with proton energies from 7.6 to 2.8 MeV.

Peak counts were calculated by subtracting neighboring background counts of the higher- and lower-energy sides of the $\gamma$-ray peaks from the gross counts of the $\gamma$-ray peaks. The detection efficiencies of the detector were determined with a $^{152}$Eu standard. The $^{145}$Eu and $^{65}$Zn activities were

TABLE I. The Gaussian-averaged cross sections and cross sections at the medians of proton energies in the $^{144}$Sm($p$, $\gamma$) $^{145}$Eu reaction determined for each $\gamma$-ray emission. The average is given by the arithmetic mean and $2\sigma$ uncertainty in the weighted average.

| Monitor stack | | | | Target stack 1 | | | | Target stack 2 | | | |
|---|---|---|---|---|---|---|---|---|---|---|---|
| $E_{c.m.}$ (keV) | $E_\gamma$ (keV) | Gaussian-averaged cross section (mb) | Cross section (median) (mb) | $E_{c.m.}$ (keV) | $E_\gamma$ (keV) | Gaussian-averaged cross section (mb) | Cross section (median) (mb) | $E_{c.m.}$ (keV) | $E_\gamma$ (keV) | Gaussian-averaged cross section (mb) | Cross section (median) (mb) |
| 7570 ± 150 | 653.5 | 18.1 ± 1.5 | 16.5 ± 1.4 | 6360 ± 190 | 653.5 | 10.03 ± 0.96 | 9.67 ± 0.92 | 6060 ± 190 | 653.5 | 4.40 ± 0.59 | 4.24 ± 0.57 |
| | 893.7 | 18.6 ± 1.5 | 16.9 ± 1.4 | | 893.7 | 9.96 ± 0.92 | 9.60 ± 0.89 | | 893.7 | 4.38 ± 0.57 | 4.22 ± 0.55 |
| | 1658.5 | 17.8 ± 1.5 | 16.2 ± 1.4 | | 1658.5 | 9.83 ± 0.95 | 9.48 ± 0.91 | | 1658.5 | 4.48 ± 0.61 | 4.32 ± 0.59 |
| | 1997.0 | 17.4 ± 1.5 | 15.8 ± 1.3 | | 1997.0 | 10.57 ± 1.08 | 10.19 ± 1.05 | | 1997.0 | 4.66 ± 0.67 | 4.49 ± 0.64 |
| | Average | 18.0 ± 1.5 | 16.4 ± 1.4 | | Average | 10.1 ± 1.0 | 9.74 ± 0.94 | | Average | 4.48 ± 0.61 | 4.32 ± 0.58 |
| | | | | 5690 ± 190 | 653.5 | 3.53 ± 0.33 | 3.47 ± 0.33 | 5370 ± 210 | 653.5 | 1.34 ± 0.18 | 1.34 ± 0.18 |
| | | | | | 893.7 | 3.55 ± 0.33 | 3.49 ± 0.32 | | 893.7 | 1.42 ± 0.19 | 1.42 ± 0.19 |
| | | | | | 1658.5 | 3.60 ± 0.34 | 3.54 ± 0.34 | | 1658.5 | 1.54 ± 0.21 | 1.54 ± 0.21 |
| | | | | | 1997.0 | 3.77 ± 0.38 | 3.70 ± 0.37 | | 1997.0 | 1.52 ± 0.22 | 1.52 ± 0.22 |
| | | | | | Average | 3.61 ± 0.34 | 3.55 ± 0.34 | | Average | 1.46 ± 0.20 | 1.46 ± 0.20 |
| | | | | 4970 ± 220 | 653.5 | 0.933 ± 0.088 | 0.920 ± 0.086 | 4620 ± 230 | 653.5 | 0.420 ± 0.057 | 0.402 ± 0.055 |
| | | | | | 893.7 | 0.905 ± 0.083 | 0.893 ± 0.082 | | 893.7 | 0.395 ± 0.052 | 0.378 ± 0.050 |
| | | | | | 1658.5 | 0.927 ± 0.089 | 0.914 ± 0.087 | | 1658.5 | 0.411 ± 0.057 | 0.393 ± 0.054 |
| | | | | | 1997.0 | 0.958 ± 0.098 | 0.945 ± 0.097 | | 1997.0 | 0.400 ± 0.061 | 0.382 ± 0.058 |
| | | | | | Average | 0.931 ± 0.089 | 0.918 ± 0.087 | | Average | 0.407 ± 0.056 | 0.389 ± 0.054 |
| | | | | 4150 ± 260 | 653.5 | 0.156 ± 0.015 | 0.149 ± 0.014 | 3750 ± 280 | 653.5 | 0.0441 ± 0.0062 | 0.0424 ± 0.0060 |
| | | | | | 893.7 | 0.155 ± 0.014 | 0.148 ± 0.014 | | 893.7 | 0.0455 ± 0.0060 | 0.0438 ± 0.0058 |
| | | | | | 1658.5 | 0.156 ± 0.015 | 0.149 ± 0.014 | | 1658.5 | 0.0509 ± 0.0072 | 0.0490 ± 0.0069 |
| | | | | | 1997.0 | 0.169 ± 0.017 | 0.162 ± 0.016 | | 1997.0 | 0.0511 ± 0.0086 | 0.0492 ± 0.0082 |
| | | | | | Average | 0.159 ± 0.015 | 0.152 ± 0.014 | | Average | 0.0479 ± 0.0068 | 0.0461 ± 0.0065 |
| | | | | 3190 ± 300 | 653.5 | 0.01009 ± 0.00125 | 0.00612 ± 0.00076 | 2810 ± 350 | 653.5 | 0.00248 ± 0.00097 | 0.000919 ± 0.000358 |
| | | | | | 893.7 | 0.00957 ± 0.00095 | 0.00580 ± 0.00058 | | 893.7 | 0.00347 ± 0.00050 | 0.001285 ± 0.000186 |
| | | | | | 1658.5 | 0.00805 ± 0.00118 | 0.00488 ± 0.00072 | | 1658.5 | 0.00440 ± 0.00100 | 0.001630 ± 0.000370 |
| | | | | | 1997.0 | 0.00883 ± 0.00257 | 0.00535 ± 0.00156 | | 1997.0 | Not detected (<0.003) | |
| | | | | | Average | 0.00914 ± 0.00124 | 0.00554 ± 0.00075 | | Average | 0.00345 ± 0.00081 | 0.00128 ± 0.00030 |

determined using Eq. (1),

$$A_0 = \frac{\lambda C}{I_\gamma \varepsilon (e^{-\lambda t_{\rm cool}} - e^{-\lambda (t_{\rm cool}+t_{\rm meas})})}, \quad (1)$$

where $A_0$ is the activity after termination of irradiation, $C$ is the peak count, $\lambda$ is the decay constant, $I_\gamma$ is the emission probability of the $\gamma$ ray, $\varepsilon$ is the detection efficiency, and $t_{\rm cool}$ and $t_{\rm meas}$ are the cooling time and measurement time, respectively. $\gamma$ rays of 1115.5 keV ($I_\gamma = 50.04\%$) for $^{65}$Zn, 653.5 keV ($I_\gamma = 15.0\%$), 893.7 keV ($I_\gamma = 66.0\%$), 1658.5 keV ($I_\gamma = 14.9\%$), and 1997.0 keV ($I_\gamma = 7.2\%$) for $^{145}$Eu were used for the analyses [23,24]. Proton flux in the irradiated monitor stack was calculated from the $^{65}$Zn activity using Eq. (2),

$$f = \frac{A_0}{\sigma N (1 - e^{-\lambda t_{\rm irr}})}, \quad (2)$$

where $\sigma$ denotes the cross section, $f$ denotes the proton flux estimated from the monitor foil, $N$ denotes the number of target atoms in a unit area, and $t_{\rm irr}$ denotes the irradiation time. Here, the $^{65}$Cu$(p,n)^{65}$Zn cross section reported by Kopecký [33] was used for the calculation. The cross section of 126 mb at the proton energy of 6.25 MeV was used for calculating the flux. Using a rearrangement of Eq. (2), the flux and $^{144}$Sm activities provided the cross section of the $^{144}$Sm$(p,\gamma)^{145}$Eu reaction in the monitor stack.

The $^{145}$Eu activity in the target stacks was determined using Eq. (1) by referring to the $^{145}$Eu activity in the monitor stack. The first $^{144}$Sm target in the target stack was expected to have the same cross section as that in the monitor stack as both targets were bombarded with equal proton energy. Cross sections of the other targets in the target stacks were determined using Eq. (2) referring to the first $^{144}$Sm target in target stack 1. Regarding the uncertainty in the cross section, we considered the uncertainty in the half-lives of $^{145}$Eu and $^{65}$Zn as well as in the thickness of the $^{144}$Sm targets, 7% uncertainty in the cross section of the $^{65}$Cu$(p,n)^{65}$Zn monitor reaction, and 1% uncertainty in the detector efficiency determined with the $^{152}$Eu standard.

## III. RESULTS AND DISCUSSION

### A. Experimental cross sections and comparison with theoretical predictions

The Gaussian-averaged cross sections determined by each $\gamma$ ray as well as the average cross sections are summarized in Table I. Each cross section determined from different $\gamma$ rays agreed within the error. The weighted mean of $2\sigma$ are considered as the uncertainty in the average value. On the other hand, a statistical count of $3\sigma$ in the background of the neighboring $\gamma$-ray peak was considered as a detection limit. The $\gamma$-ray peak of 1997.0 keV for 2.8-MeV irradiation did not exceed the detection limit. In the present paper, $^{144}$Sm$(p,\gamma)^{145}$Eu cross sections down to 3.45 $\mu$b were successfully determined.

The $^{144}$Sm$(p,\gamma)^{145}$Eu cross sections are compared in Fig. 3 with theoretical predictions obtained using the Hauser-Feshbach statistical codes NON-SMOKER [18] and TALYS1.6

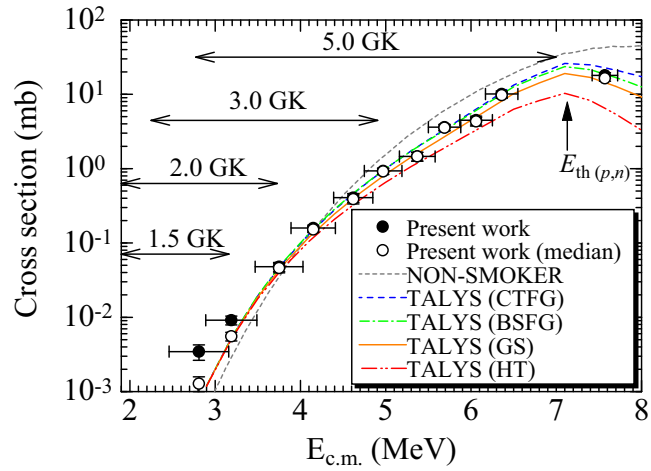


FIG. 3. The experimental cross sections and theoretical cross sections obtained using NON-SMOKER and TALYS. $E_{\rm th\,(p,n)}$ denotes the threshold of the $^{144}$Sm$(p,n)^{145}$Eu reaction. The experimental cross sections corrected based on TALYS using the GS model are shown with an open circle. Regions of the Gamow peak covering $2\sigma$ (95%) of the area at temperatures between 1.5 and 5.0 GK are shown with arrows.

[34]. In addition, energy regions which cover approximately $2\sigma$ (95%) of the Gamow peak are illustrated with arrows (details are given in Sec. III B). The present paper encompassed nucleosynthesis temperatures between 3 and 5 GK. Extrapolation of the cross sections is required to calculate reaction rates in a stellar environment at temperatures lower than 3 GK.

We employed one mass model for NON-SMOKER and four level-density models for the TALYS calculations. The finite range droplet model was used as the mass model for the NON-SMOKER calculation [35]. The constant temperature Fermi-gas (CTFG) model, backshifted Fermi-gas (BSFG) model, generalized superfluid (GS) model, and microscopic level densities from Hilaire's combinatorial tables (HT) were used for the level-density model in the TALYS calculation [36,37]. The NON-SMOKER calculation produced greater values of the cross sections than that obtained from measurements at energies higher than 4 MeV and smaller values than those obtained from experimental measurements at energies lower than 4 MeV. As seen in the comparison of the experimental cross sections with the theoretical predictions (Fig. 3), the $\chi^2$ values per degree of freedom between 3.8 and 7.6 MeV are estimated to be 0.44 for TALYS using the CTFG model, 0.17 for the BSFG model, 0.043 for the GS model, 1.6 for the HT, and 3.2 for the NON-SMOKER model. The TALYS calculations using the GS model show the best agreement with the experimental values at energies between 3.8 and 7.6 MeV. The competing $^{144}$Sm$(p,n)^{144}$Eu reaction channel occurs at energies higher than 7.129 MeV. The $^{144}$Sm$(p,\gamma)^{145}$Eu reaction calculated using TALYS, based on the GS model, agreed well with experimental values even at energies higher than the threshold of the $(p,n)$ reaction.

In the present paper, we used thick degrader foils; hence, a large spread in the energies of the proton beams would have

been present after each foil. Here, we take this large energy spread into account when calculating the cross sections by calculating a weighted average of the cross sections using a Gaussian distribution for the proton energies. As described in Sec. II C, the median proton beam energies were estimated with SRIM [22], and the extent of the proton energy ranges due to straggling were determined using PHITS [30] using ATIMA [31,32]. The SRIM median proton energies after each foil were assigned to be the mean of a Gaussian proton energy distribution, and the width of that distribution was assigned to be the minimum and maximum proton energies as determined with PHITS + ATIMA. Gaussian-averaged cross sections could then be calculated by taking the convolution of the Gaussian proton energy distribution for each energy and the values of the cross section over that same energy range. This produced an effective proton energy, which corresponded with our measured cross sections but differed from the median proton energies from SRIM. In order to adjust the cross sections to the median proton energy instead, the experimental cross sections were renormalized using the ratio of the theoretical cross sections as determined using TALYS with the GS model at the effective and median proton energies. If the form of the cross section is particularly steep in a given energy range as it is at the lower proton energies observed, the adjustment between the effective and the median proton energies is larger as seen in the data. The result of this renormalization, from the effective to the median proton energies, is apparent in the shift of the data points in Fig. 3.

The cross sections at the median proton energies are 37% of the Gaussian-averaged cross section at 2.8 MeV, 61% at 3.2 MeV, and 90%–100% at energies higher than 3.8 MeV. The cross sections at the medians are also summarized in Table I. The cross sections at 2.8 and 3.2 MeV were greater than theoretical values calculated using TALYS by a factor of ∼1.5. The GS model agrees well with the renormalized cross sections over the investigated energy with the $\chi^2$ value per degree of freedom of 0.042. In the following discussion, the cross sections at the median proton energies are used.

The sensitivity is generally useful to understand what input parameter in a model contributes to magnitude of the cross sections. The sensitivity of the $^{144}$Sm$(p,\gamma)$ $^{145}$Eu cross section in the Hauser-Feshbach model is shown in Fig. 4 where the ratio of quantities $v_q$ in Eq. (3) is assumed to be 2, which is the same magnitude of difference as the $^{130}$Ba$(p,\gamma)$ $^{131}$La reaction [20]. The sensitivity $\Omega_{S_q}$ is defined as

$$\Omega_{S_q} = \frac{v_\Omega - 1}{v_q - 1}, \tag{3}$$

$v_\Omega$ is the ratio of cross sections using modified and conventional parameters when the proton width, $\gamma$ width, neutron width, and $\alpha$ width are separately changed. $v_q$ denotes the ratio of the modified to the conventional average widths [38]. The sensitivity value reveals which parameter more strongly affects the final result. For example, a sensitivity $\Omega_{S_q} = 0$ denotes no change in the cross section even when the widths are varied. On the other hand, $\Omega_{S_q} = 1$ indicates that the cross section changes by the same factor as $v_q$ when the widths are changed.

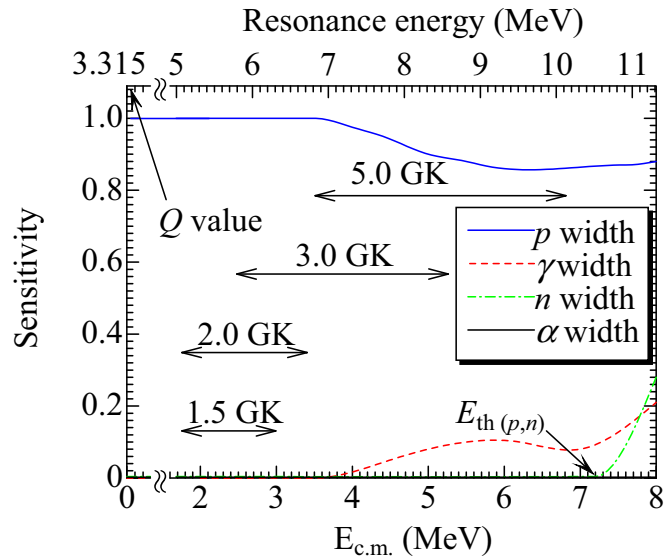


FIG. 4. Sensitivity of the $^{144}$Sm$(p,\gamma)$ $^{145}$Eu reaction when the proton width, $\gamma$ width, neutron width, and $\alpha$ width are separately changed by a factor of 2. The arrows indicate energy regions of the Gamow peak covering $2\sigma$ (95%) of the area. Resonance energies of $^{145}$Eu, equivalent to the sum of the $Q$ value of the $^{144}$Sm$(p,\gamma)$ $^{145}$Eu reaction and center-of-mass energy of the proton beams, are related to the incident energies.

Figure 4 clearly reveals that the proton width is the dominant factor in determining the $^{144}$Sm$(p,\gamma)$ $^{145}$Eu cross-sectional value at the astrophysically relevant energies of 1–7 MeV. At energies higher than ∼4 MeV, the $\gamma$ width contributes to the cross section as well. In addition, the neutron width contributes at energies higher than the threshold of the $^{144}$Sm$(p,n)$ $^{144}$Eu reaction. In the $^{144}$Sm$(p,\gamma)$ reaction, the theoretically predicted cross sections agree well with the experimental cross sections without correction of the proton widths at 2.8–7.6 MeV. In addition, no correction of the neutron widths is required at energies higher than the threshold of the $^{144}$Sm$(p,n)$ reaction. TALYS uses the phenomenological optical model potential when a default input is employed [39]. In the $^{144}$Sm$(p,\gamma)$ $^{145}$Eu reaction, the GS model for a level density and the phenomenological optical model potential with the default proton widths give the best cross sections.

There are additional instances in the literature of measured proton capture cross sections displaying an energy-dependent agreement with Hauser-Feshbach calculations. For example, Quinn *et al.* [40] reported that the experimental cross sections of the $^{74}$Ge$(p,\gamma)$ $^{75}$As reaction showed good agreement with TALYS using the CTFG model at energies higher than 2 MeV. In contrast, the cross sections calculated using NON-SMOKER were approximately 50% less than the experimental values. However, the NON-SMOKER calculation showed good agreement at energies lower than 2 MeV. Spyrou *et al.* [41] reported that both a TALYS calculation employing the GS model and a NON-SMOKER calculation of the $^{90}$Zr$(p,\gamma)$ $^{91}$Nb reaction cross section agreed well with experiment at energies between 2.5 and 5 MeV. In addition, the $^{93}$Zr$(p,\gamma)$ $^{93}$Nb reaction showed good agreement with NON-SMOKER

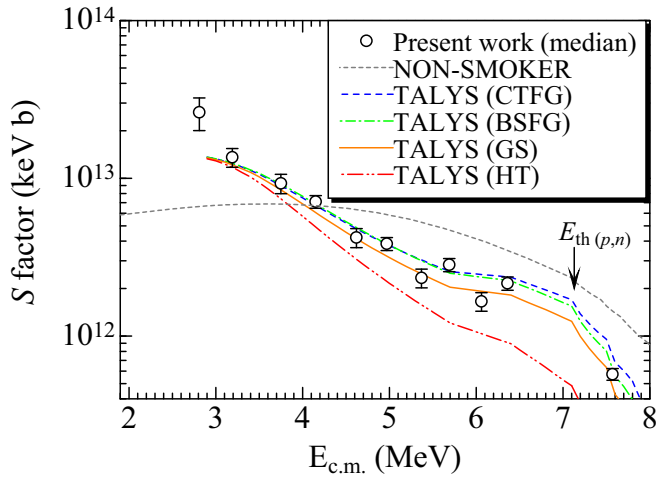


FIG. 5. The astrophysical $S$ factors of the $^{144}$Sm$(p,\gamma)$ $^{145}$Eu reaction calculated from the experimental cross sections and theoretical predictions using NON-SMOKER and TALYS employing CTFG, BSFG, GS, and HT as a level-density model.

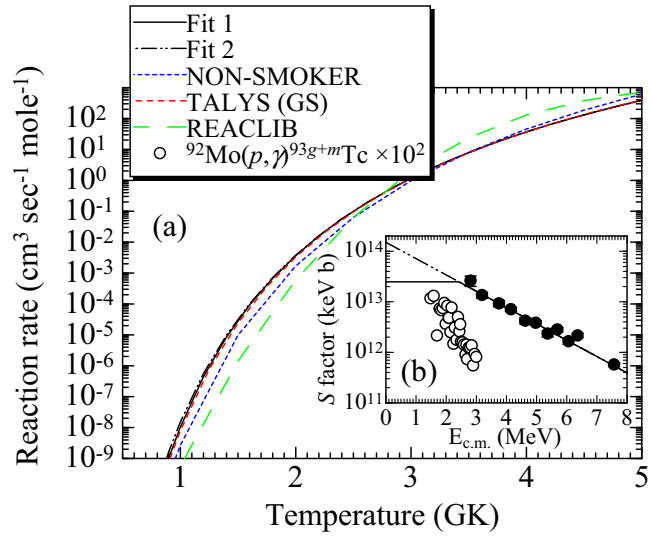


FIG. 6. (a) The reaction rates estimated from the different extrapolations and theoretical predictions using NON-SMOKER, TALYS, and REACLIB. (b) Demonstration of the different fits used to extrapolate the measurement to lower energies and the $S$ factors of the $^{92}$Mo$(p,\gamma)^{93m+g}$Tc reaction multiplied by 100. In Fit 1, a constant value taken from the lowest datum is used; for Fit 2 an exponential form based on the higher energy data was assumed. See the text for a further discussion.

calculations. Gyürky *et al.* [42] reported measurements of $(p,\gamma)$ reactions on the proton-rich nuclei of $^{106}$Cd and $^{108}$Cd. Both experimental cross sections were higher than the NON-SMOKER calculations by 50% at energies lower than ∼3.5 MeV. Netterdon *et al.* [20] compared the experimental cross sections of $^{130}$Ba$(p,\gamma)$ $^{131}$La with those obtained via TALYS. The TALYS calculation, using the default parameters, presented smaller cross sections than measurement data in the range of 3.6–5.0 MeV. The discrepancies observed in these nuclear reactions were solved by employing an appropriate optical model potential and level density and correcting the proton and neutron widths.

### B. Reaction rate in the stellar environment estimated from the $S$ factor

The astrophysical $S$ factor of the $^{144}$Sm$(p,\gamma)$ $^{145}$Eu reaction is shown in Fig. 5 together with those estimated using NON-SMOKER and TALYS. The astrophysical $S$ factor $S(E)$ is expressed as

$$S(E) = E\sigma(E)e^{2\pi\eta}, \tag{4}$$

where $E$ is the center-of-mass system energy, $\sigma(E)$ is the cross section, and $\eta$ is the Sommerfeld parameter expressed as $Z_1 Z_2 e^2/\hbar v$. $Z_1$ and $Z_2$ are the atomic numbers of the interacting nuclei, $e$ is the elementary charge, and $v$ is the relative velocity in the reaction. The $S$ factor estimated with TALYS when using the GS model shows the best agreement with the experimental data as well as comparison in the cross sections. The $S$ factor decreases exponentially with an increase in energy.

Proton capture reaction rates in the stellar plasma temperature are expressed using the $S$ factor as in Eq. (4),

$$N_A\langle\sigma v\rangle = N_A \frac{(8/\pi)^{1/2}}{\mu^{1/2}(kT)^{3/2}} \int_0^\infty S(E)e^{-2\pi\eta - E/kT}dE, \tag{5}$$

where $N_A$ is the Avogadro number, $\mu$ is the reduced mass of the system, $k$ is the Boltzmann constant, and $T$ is the temperature [43]. Here, we presume two scenarios to predict the $S$ factors at energies lower than 2.8 MeV where the cross sections were not experimentally measured. When we estimated the $S$ factor of the $(p,\gamma)$ reaction on $^{92}$Mo, another neutron-magic nucleus, the $S$ factor was found to be almost constant at energies lower than 1.8 MeV, decreasing steeply at energies between 1.8 and 3 MeV and decreasing gently at energies higher than 3 MeV [44,45] [Fig. 6(b)]. This trend observed at energies higher than 1.8 MeV is identical to that observed in the $^{144}$Sm$(p,\gamma)$ $^{145}$Eu reaction. In the first scenario, the $S$ factors were extrapolated according to the trends observed in the $^{92}$Mo$(p,\gamma)$ $^{93}$Tc reaction. The $S$ factors at energies higher than 2.8 MeV were fitted with an exponential function, and the $S$ factor at energies below 2.8 MeV was assumed to be of the same value as that at 2.8 MeV (Fit 1). In the second scenario, the $S$ factors at energies higher than 2.8 MeV were fitted with the same exponential function as for Fit 1, and the $S$ factors from 0 to 2.8 MeV were extrapolated using this exponential function (Fit 2).

The proton capture reaction rates for the ground state $^{144}$Sm atom were estimated using both fitting values. Figure 6(a) displays the reaction rates measured in the laboratory environment together with those estimated using NON-SMOKER and TALYS. The GS model was employed in the TALYS calculation. In addition, the Hauser-Feshbach model reaction rates from the REACLIB database are presented [46]. The features of each fit are shown in Fig. 6(b). Figure 7 displays the ratios of the experimental reaction rates to the NON-SMOKER, TALYS, and REACLIB reaction rates. As mentioned in Sec. III A,

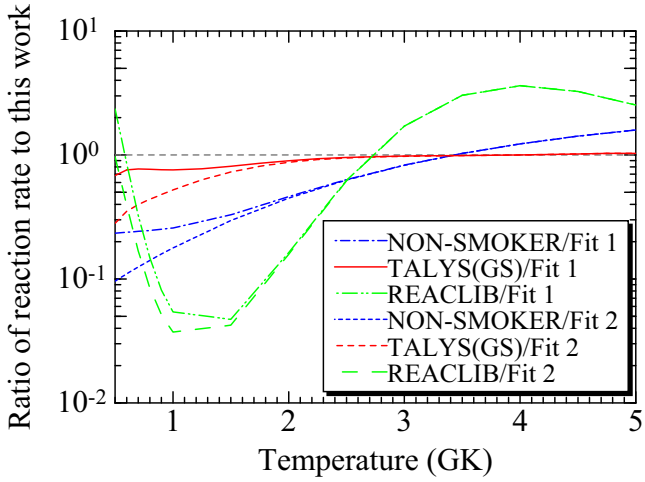


FIG. 7. Ratios of the reaction rates using theoretical predictions using NON-SMOKER, TALYS, and REACLIB for the data estimated using two different extrapolations. The gray broken line indicates the ratio as 1.0.

the corrected experimental cross sections agreed with the cross sections calculated using TALYS with the GS model at energies between 2.8 and 7.6 MeV. The NON-SMOKER cross sections revealed greater values above 3.8 MeV. The NON-SMOKER calculations produced values smaller than the measurement data at energies lower than 3.8 MeV. Hence, the ratios of the reaction rates to NON-SMOKER theoretical data were greater at temperatures higher than 3.5 GK and smaller at temperatures lower than 3.5 GK. The REACLIB rate is weaker than in the present paper at temperatures between 1 and 2 GK by a factor of ∼20 and even larger factors for temperatures higher than 3 GK. Comparing with the TALYS calculation, we confirmed the reaction rates calculated using TALYS correspond to those estimated from experimental cross sections by a factor of less than 1.1 at temperatures higher than 2.5 GK. At temperatures lower than 2.5 GK, the extrapolation of the $S$ factor results in different reaction rates. The reaction rate in the stellar environment at temperatures lower than 2.5 GK should be greater than that in both theoretical computations employing the Hauser-Feshbach model. In the present paper, $^{144}$Sm$(p,\gamma)$ $^{145}$Eu experimental cross sections were compared with theoretical data obtained using NON-SMOKER and TALYS to understand which factors in a nuclear model cause differences between measurement and theoretical values.

The nucleosynthesis of $^{144}$Sm by the reactions of $(p,\gamma)$ and $(p,n)$ on the preexisting $s$ nuclei of Nd isotopes, reaction products of Pm isotopes, and $^{144}$Sm have been assumed in temperatures of 1.5–3.5 GK [6,7]. At the temperatures, the estimated reaction rates from theoretical calculations with TALYS based on the GS model correspond to those from the experimental measurements within a factor of 2. In the network calculation of nucleosynthesis, the final abundance of $^{144}$Sm in the proton capture reaction can be estimated using the balance between rates of increase caused by the $(p,\gamma)$ reaction on existing Nd and Pm and the rate of decrease caused by the $^{144}$Sm$(p,\gamma)$ $^{145}$Eu reaction. The experimental cross sections are only one part of a broader network controlling $^{144}$Sm abundance. In order to perform an accurate network calculation, we require cross sections predicted using a Hauser-Feshbach statistical calculation where inputs of level density and optical model potential, etc., are optimized by comparing with experimental cross sections. A further study of the $(p,\gamma)$ and $(p,n)$ reactions on Nd and Pm isotopes would fill in the missing pieces of the network reaction surrounding $^{144}$Sm.

## IV. CONCLUSION

We measured the cross sections of the proton capture reactions on $^{144}$Sm atoms at energies between 2.8 and 7.6 MeV. Irradiation by a proton beam was carried out at RCNP, Osaka University, and the activities of $^{145}$Eu were determined with $\gamma$-ray spectrometry. At energies higher than 3.8 MeV, the experimental cross sections agreed well with the theoretical prediction when using TALYS which employs the generalized superfluid model for level densities. When the overestimations by the large energy uncertainties are taken into account, the experimental cross sections showed comparable values to TALYS but higher than NON-SMOKER. The TALYS calculation employing the GS model reproduced well the experimental cross section without correction of the proton widths at energies between 2.8 and 7.6 MeV. The experimental cross sections at 2.8–7.6 MeV included the Gamow peak at temperatures between 3 and 5 GK. The cross sections in the present paper provided a value of the $(p,\gamma)$ reaction rate on the ground state of $^{144}$Sm. The reaction rates at temperatures higher than 2.5 GK agreed with the TALYS calculation employing the GS model within 10%. However, the reaction rates at temperatures lower than 2.5 GK were estimated to be greater than the theoretical predictions when the $S$ factor was extrapolated at energies lower than 2.8 MeV. The reaction rate at temperatures below 2.5 GK were more sensitive to the choice of extrapolation of the cross sections. The reaction rate estimated by TALYS employing the GS model showed an uncertainty within a factor of 2 at 1.5–3.5 GK for typical temperatures of the nucleosynthesis of the $p$ nuclei.

## ACKNOWLEDGMENTS

We wish to acknowledge the assistance of the staff of RCNP, Osaka University with regard to proton irradiation. This work was supported, in part, by Japan Society for the Promotion of Science (JSPS) KAKENHI Grant No. 26800161.

[1] M. Arnould, S. Goriely, and K. Takahashi, Phys. Rep. **450**, 97 (2007).

[2] F. Käppeler, R. Gallino, S. Bisteryo, and W. Aoki, Rev. Mod. Phys. **83**, 157 (2011).

[3] M. Rayet, N. Prantzos, and M. Arnould, Astron. Astrophys. **227**, 271 (1990).
[4] T. Rauscher, A. Heger, R. D. Hoffmann, and S. Woosley, Astrophys. J. **576**, 323 (2002).
[5] H. Utsunomiya, P. Mohr, A. Zilges, and M. Rayet, Nucl. Phys. **A777**, 459 (2006).
[6] C. Travaglio, F. K. Röpke, R. Gallino, and W. Hillebrandt, Astrophys. J. **739**, 93 (2011).
[7] H. Schatz *et al.*, Phys. Rep. **294**, 167 (1998).
[8] C. Fröhlich, G. Martínez-Pinedo, M. Liebendörfer, F.-K. Thielemann, E. Bravo,W. R. Hix, K. Langanke, and N. T. Zinner, Phys. Rev. Lett. **96**, 142502 (2006).
[9] T. Plewa, A. C. Calder, and D. Q. Lamb, Astrophys. J. **612**, L37 (2004).
[10] W. Rapp, J. Görres, and M. Wiescher, Astrophys. J. **653**, 474 (2006).
[11] J. Magill, G. Pfenning, and J. Galy, *Chart of the Nuclides,* 8th ed. (EC-DG JRC-ITE, Karlsruhe, Germany, 2012).
[12] M. E. Wieser and J. R. De Laeter, Phys. Rev. C **75**, 055802 (2007).
[13] T. L. Chang, M. T. Zhao, W. J. Li, J. Wang, and Q. Y. Qian, Int. J. Mass Spectrom. **218**, 167 (2002).
[14] T. Hayakawa, T. Shizuma, T. Kajino, K. Ogawa, and H. Nakada, Phys. Rev. C **77**, 065802 (2008).
[15] T. Hayakawa, K. Nakamura, T. Kajino, S. Chiba, N. Iwamoto, M. K. Cheoun, and G. J. Mathews, Astrophys. J. Lett. **779**, L9 (2013).
[16] M. Arnould and S. Goriely, Phys. Rep. **384**, 1 (2003).
[17] E. Somorjai *et al.*, Astron. Astrophys. **333**, 1112 (1998).
[18] T. Rauscher and F. K. Thielemann, At. Data Nucl. Data Tables **79**, 47 (2001).
[19] C. Nair *et al.*, Phys. Rev. C **81**, 055806 (2010).
[20] L. Netterdon, A. Endres, G. G. Kiss, J. Mayer, T. Rauscher, P. Scholz, K. Sonnabend, Z. Török, and A. Zilges, Phys. Rev. C **90**, 035806 (2014).
[21] W. Parker, H. Bildstein, N. Getoff, H. Fischer-Colbrie, and H. Regal, Nucl. Instrum. Methods **26**, 61 (1964).
[22] J. F. Ziegler, M. D. Ziegler, and J. P. Biersack, Nucl. Instrum. Methods Phys. Res., Sect. B **268**, 1818 (2010).
[23] E. Browne and J. K. Tuli, Nucl. Data Sheets **110**, 507 (2009).
[24] E. Browne and J. K. Tuli, Nucl. Data Sheets **111**, 2425 (2010).
[25] D. C. Aumann and G. Müllen, Nucl. Instrum. Methods **115**, 75 (1974).
[26] M. Fukuda, K. Hatanaka, H. Kawamata, T. Yorita, T. Saito, H. Tamura, and M. Kibayashi, Proceedings of IPAC'10, Kyoto, Japan, 2010, (IPAC'10 OC/ACFA, 2010), p. 546, paper no. MOPEC039.
[27] H. Sørensen and H. H. Andersen, Phys. Rev. B **8**, 1854 (1973).
[28] H. H. Andersen, J. F. Bak, H. Knudsen, and B. R. Nielsen, Phys. Rev. A **16**, 1929 (1977).
[29] H. H. Andersen, H. Simonsen, H. Sørensen, and P. Vajda, Phys. Rev. **186**, 372 (1969).
[30] T. Sato *et al.*, J. Nucl. Sci. Technol. **50**, 913 (2013).
[31] O. B. Firsov, Sov. Phys. JETP **5**, 1192 (1957).
[32] P. Hvelplund, Mat. Fys. Medd. Dan. Vid. Selsk **38**, 4 (1971).
[33] P. Kopecký, Int. J. Appl. Radiat. Isot. **36**, 657 (1985).
[34] A. J. Koning, S. Hilaire, and M. C. Duijvestijn, in *Proceedings of the International Conference on Nuclear Data for Science and Technology, April 22–27, 2007, Nice, France*, edited by O. Bersillon, F. Gunsing, E. Bauge, R. Jacqmin, and S. Leray (EDP Sciences, France, 2008), pp. 211–214.
[35] P. Möller, J. R. Nix, W. D. Myers, and W. J. Swiatecki, At. Data Nucl. Data Tables **59**, 185 (1995).
[36] A. J. Koning, S. Hilaire, and S. Goriely, Nucl. Phys. **A810**, 13 (2008).
[37] S. Goriely, S. Hilaire, and A. J. Koning, Phys. Rev. C **78**, 064307 (2008).
[38] T. Rauscher, Astrophys. J. Suppl. Ser. **201**, 26 (2012).
[39] A. J. Koning and J. P. Delaroche, Nucl. Phys. **A713**, 231 (2003).
[40] S. J. Quinn *et al.*, Phys. Rev. C **88**, 011603(R) (2013).
[41] A. Spyrou *et al.*, Phys. Rev. C **88**, 045802 (2013).
[42] Gy. Gyürky, G. G. Kiss, Z. Elekes, Zs. Fülöp, E. Somorjai, and T. Rauscher, J. Phys. G: Nucl. Part. Phys. **34**, 817 (2007).
[43] C. Angulo *et al.*, Nucl. Phys. **A656**, 3 (1999).
[44] T. Sauter and F. Käppeler, Phys. Rev. C **55**, 3127 (1997).
[45] Gy. Gyürky, M. Vakulenko, Zs. Fülöp, Z. Halász, G. G. Kiss, E. Somorjai, and T. Szücs, Nucl. Phys. **A992**, 112 (2014).
[46] R. H. Cyburt *et al.*, Astrophys. J. Suppl. Ser. **189**, 240 (2010).